Investigations of combustion characteristics and mechanism of backfire-induced super-knock in a turbocharged hydrogen engine

Xiang-yu Li [a], Bai-gang Sun [a, b], Shi-wei Zhang [a], Ling-zhi Bao [a, c *], Qing-he Luo [a, b *], Felix Leach [c], Yan-zhong Zhang [d]

a School of Mechanical Engineering, Beijing Institute of Technology, Beijing 100081, China

b Beijing Institute of Technology Chongqing Innovation Center, Chongqing, 401121, China

c Department of Engineering Science, University of the Oxford, Oxford, OX1 3PJ, UK

d Faculty of Information Technology, Beijing University of Technology, Beijing 100124, China

Corresponding: Ling-zhi Bao (Email: paul.bao@eng.ox.ac.uk), Qing-he Luo (Email: luoqinghe@bit.edu.cn)

Abstract

Hydrogen internal combustion engines have been demonstrated to offer high power with zero carbon emissions. However, knock pose a significant obstacle to enhancing hydrogen engine performance further. Super knock commonly occurs in highly boosted engines with low-speed pre-ignition regimes while a critical super-knock induced by backfire with a new mechanism is detected in hydrogen engines. Experiments and multi-cycle numerical simulations are conducted on a 5.13 L port fuel injection turbocharged hydrogen engine. The results indicate that backfire leads to a maximum pressure amplitude oscillation of 134.7 bar super-knock in the next cycle, which is attributed by twice auto-ignition at -1.3/3.6 °CA. Backfire rises the local temperature to 915 K at the bottom of the cylinder and scrambled hydrogen distribution, leading to large locally rich regions of lambda=1.2, a lean mixture of lambda=2.9 near the spark plug, results in $5.4\times10^{-4}/2\times10^{-3}$ maximum mass fraction of HO_2/H_2O_2. The mechanism of super-knock induced by backfire and

normal knock caused by advanced ignition are compared, the unburned region size is positively correlated with the knock intensity. This study of super-knock induced by backfire mechanism is first proposed and it reveals insights of avoiding super-knock, thereby achieving higher performance hydrogen engines.

Keywords: Hydrogen engine, Abnormal combustion, Knock, Backfire

Nomenclature：

PFI	port fuel injected
DI	direct-injected
H_2ICE	hydrogen internal combustion engine
λ	excess air ratio
BMEP	brake mean effective pressure
BFSC	brake specific fuel consumption
BTE	brake thermal efficiency
IMEP	indicated mean effective pressure
ITE	indicated thermal efficiency
SOI	start of Injection
KOCA	knock onset crank angle
MAPO	maximum amplitude of pressure oscillation
TKE	turbulence kinetic energy

1. Introduction

With the development of society, environmental issues caused by the extensive application of fossil fuels have gradually emerged[1]. For sustainable development and reducing carbon emissions, carbon-free hydrogen energy has been widely popularized and applied in transportation and industry[2,3]. In addition, the hydrogen internal combustion engine (H_2ICE) has broad prospects in the field of hydrogen energy applications because of its benefits such as low hydrogen quality requirements, low cost, and zero carbon emissions[4,5].

To pursue higher thermal efficiency and greater power of hydrogen engines, a series of researchers have studied performance improvement. Golisano et al.[6] optimized the power system in a State-of-the-Art V8

6.6 L port fuel injection (PFI) hydrogen engine, knock and backfire were avoided by reducing the compression ratio and intake air temperature, and results indicated that maximum power could reach 277 kW (~42 kW/L). Tsujimura et al.[7] conducted large-sized hydrogen engine development in a 1.3 L single-cylinder direct injection (DI) hydrogen engine, they found that EGR can reduce the emissions of NOx and the tendency to knock. Their engine achieved an indicated mean effective pressure (IMEP) of 1.64 MPa with NOx emissions under 100 ppm and an indicated thermal efficiency (ITE) of over 50% by adopting the Atkinson/Miller cycle, increasing intake boost pressure, and using exhaust gas recirculation (EGR). Fischer et al.[8] investigated the operation of a 1 L 3-cylinder DI hydrogen engine; their results also showed that the Atkinson cycle and EGR can reduce knock tendency and increase engine efficiency. Bao et al.[9] optimized the performance of a 2.0 L turbocharged direct-injection hydrogen engine; their results indicated that a peak power of 120 kW and a maximum torque of 340 Nm can be achieved with a well-matched turbocharger and brake thermal efficiency (BTE) reaching 42.6% by lean combustion.

Abnormal combustion, especially knock at high loads, limited performance improvements in the above studies. Research on knock is crucial for further enhancing the performance of H_2ICE, as knock imposes significant limitations. Knock occurs when conditions ahead of the flame front result in one or more autoignition events in the end gas. High knock intensity will destroy the boundary layer of the cylinder wall, resulting in worse combustion characteristics with ultra-high peak pressures, higher fuel consumption, and even damage to the cylinder[10,11]. For hydrogen engines, the tendency to knock is even larger compared to other fueled spark ignition engines[12], due to the characteristics of low ignition energy and large flammability range of hydrogen[13,14]. Meanwhile, rich hydrogen combustion is demonstrated as more

prone to knock[15] compared to gasoline. Therefore, it is worth investigating the mechanism of knock that occurs in hydrogen engines.

In the literature, there are extensive surveys on the characteristics of hydrogen knock. Hu et al.[16] researched the performance of a 1.48 L DI hydrogen engine, they found that knock is more sensitive to excess air-fuel ratio (λ) at higher load with a limited λ of 2.3 at 11.6 bar BMEP. Ji et al.[17] studied the effect of injection strategy on knock characteristics in a hydrogen rotary engine, they proposed that two-stage direct injection can effectively reduce the tendency and intensity of knock. Wang et al.[18] investigated the knock boundary of a turbocharged direct-injection hydrogen engine; the results indicated that λ was limited by knock to 1.40 at 2500 rpm but rises to 1.80 at 4500 rpm. Meanwhile, numerical simulation methods also play an important role in explaining the experimental phenomena and knock mechanisms since they can directly describe the combustion process. Li et al.[19] studied the effects of λ on knock under different compression ratios in DI H_2ICE, and found that a high compression ratio can amplify the effect of λ on knock. When the compression ratio was 17.5, knock intensity (KI) increased from 0.4 to 7.2 MPa as λ changed from 3.3 to 2.8. Ye et al.[20] studied the effect of injection timing on knock in a DI H_2ICE by simulation; the results showed that knock intensity decreases first and then increases with injection timing retardation. Li et al.[21] investigated knock formation mechanisms in DI H_2ICE; the numerical results illustrated that H_2O_2 and HO_2 radicals play a significant role in knock flame development, and H_2ICE knock is caused by the mutual promotion of both the flame and a pressure wave. A study of autoignition and knock combustion modes with different initial temperatures and pressures of hydrogen-air mixture was illustrated by Chen et al.[22]; both autoignition and knock tended to increase with the increase of initial temperature and pressure. Chen et al. found that when the initial pressure is 10 atm, when the initial temperature increases from 900K to 1000K

and 1100K, autoignition and knock occur respectively. Hong et al.[23] investigated the effects of miller cycle and oxygen-enriched atmosphere on knock characteristics on a DI hydrogen engine, and found that the deep miller cycle strategy can suppress knock intensity. However, the above research is more focused on knock phenomenon, there has been limited focus on the relationships among abnormal combustion.

A PFI hydrogen engine offers the advantages of easy modification from an existing base engine, high hydrogen flow, and is widely used in large-bore heavy-duty applications[24–26]. However, in addition to knock, other abnormal combustion also constrained the development of PFI hydrogen engine such as preignition and backfire. Preignition is a stochastic premature abnormal combustion by surface ignition[27], which could increase mechanical load of engine and even cause irreversible damage[28,29]. Furthermore, backfire is a common abnormal combustion phenomenon in PFI hydrogen engines and can cause damage and destruction to the inlet system and injector, and has a great impact on the engine performance[30]. Backfire is influenced by engine operating parameters, such as intake temperature[31], mixture concentration[32], SOI (Start of Injection)[33], valve overlap angle[34,35], amongst other things. Researchers have also studied knock after backfire. Luo et al[36] studied the inducing factors of combustion knock in a PFI hydrogen engine; their experimental results illustrated that backfire was an important factor of knock occurrence, which increases the possibility of knock by increasing the initial temperature at ignition. Dhyani et al.[37] carried out an experimental study analyzing the influence of backfire on knock in a hydrogen spark ignition engine and found that knock can be linked with backfire, and that a high equivalence ratio (0.82) could cause the low-intensity backfire which promotes knock occurrence. Marwaha et al.[38] carried out an experimental and optimal study analyzing the occurrence, duration, and termination of backfire in a hydrogen-fueled automotive spark ignition engine. Menaa et al.[34] optimized the injection system and

valve lifting law by hydrogen engine simulation. However, the numerical investigation focused on the optimization with less backfire phenomenon. Above all, previous studies on tempering have primarily been experimental, with relatively few simulation-based investigations, the characteristics of backfire need to be further elucidated through more simulation research.

In summary, most research has focused on the backfire phenomenon, and less emphasis is placed on the study of subsequent cycles after a backfiring cycle. However, a critical super-knock induced by backfire with a new mechanism is detected in large-bore PFI hydrogen engines. In addition, it is worth further investigating the relationship between these two abnormal combustion phenomena. Therefore, combustion characteristics of a 5.13 L PFI hydrogen engine are investigated in this paper. The difference between the normal knock induced by advancing ignition timing and super-knock after backfire is illustrated. Mechanisms of knock are revealed by mixture distribution, in- cylinder flow, and elementary reaction studies.

2. Method

2.1 Experimental setup

Experiments are conducted on a modified 5.13 L turbocharged four-cylinder PFI hydrogen engine based on the Yuchai K05 engine. The engine specifications are shown in Table 1, showing a high compression ratio of 12.5 and with a well-matched turbocharger. The camshaft is redesigned to reduce the valve overlap in order to avoid backfire directly ignited by hot exhaust gases. Four Delphi PFI hydrogen injectors with an injection pressure range from 15 to 30 bar are installed on the manifold toward the intake valves.

Table 1 Engine parameters.

Parameters	Value

Bore (mm)	110
Stroke (mm)	135
Rod length (mm)	215
Compression ratio	12.5
Number of cylinders	4
Displacement (L)	5.132
Engine speed range(rpm)	800~2000

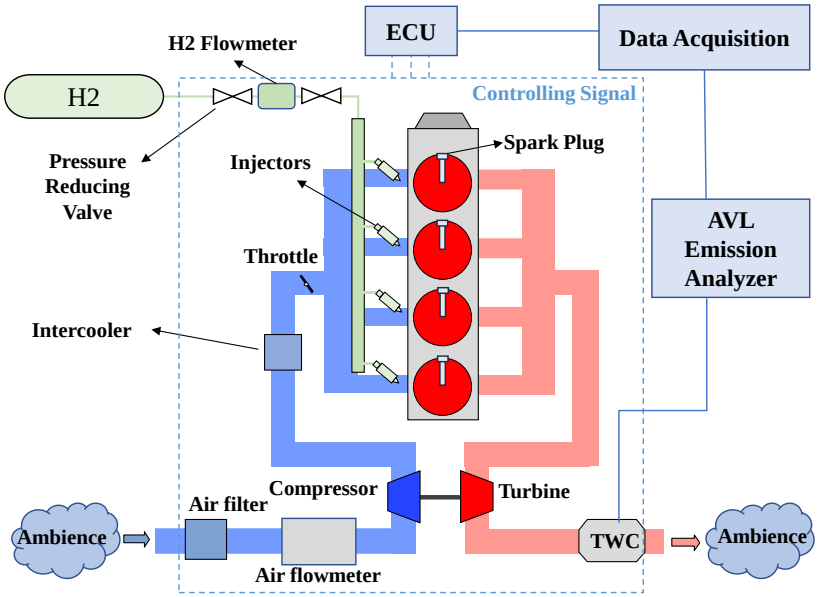
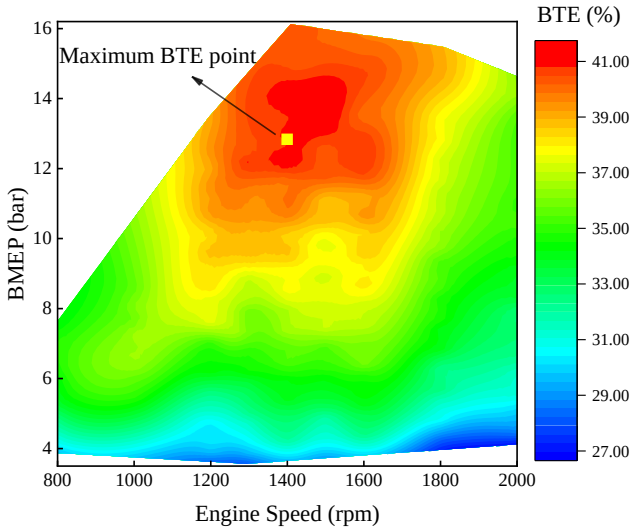


Figure 1 Schematic diagram of the PFI hydrogen engine

Table 2 The measuring devices and data accuracy.

Parameters	**Devices**	**Accuracy**
Speed	GW250 dynamometer	±1rpm
Torque	FC2000 Torque transducer	±1Nm
Cylinder Pressure	Kistler 6177B sensor	±0.02MPa
Intake/Exhaust Pressure	Kistler 4080B sensor	±0.001MPa
Air mass flow	MTR-500 Air flowmeters	±2.5kg/h
Hydrogen mass flow	CMF010 H2 flowmeters	±0.01kg/h

123 The schematic diagram of the test bench is shown in Figure 1, and the measuring devices and accuracy are
124 shown in Table 2. A CW250 eddy current dynamometer is included in the engine test system. An Emerson
125 CMF010 Coriolis mass flow meter is used to determine the hydrogen mass flow. The Kibox combustion
126 analyzer is used in the data acquisition system. Kistler 6177B sensor and Kistler 4080B sensor are used to
127 record the cylinder pressure and transient intake and exhaust pressure, respectively. The engine is warmed
128 up before testing to ensure that the oil and cooling water reach temperatures of 90°C and 80°C, respectively.
129 Engine performance tests are carried out by modifying the ignition timing under different engine speed and
130 load conditions. After the hydrogen engine had stabilized at the operating point for 2 min, the average value
131 of the test data for 220 cycles is measured and recorded.
132



133

134 Figure 2 Test results of BFSC working map of PFI hydrogen engine

135

136 The experimental results of our previous work[39] demonstrated that the engine's characteristics showed
137 a peak torque of 662 Nm and a maximum power of 129 kW, and the BTE characteristics with BMEP of
138 experiments are shown in Figure 2. However, a series of consecutive abnormal cycles among 220 cycles are

observed when operating in the high BTE and BMEP at an engine speed of 1400 rpm, including a backfire cycle and a super-knock cycle induced by the previous backfire cycle. Therefore, the operating condition at the maximum BTE point of 41.2% is selected as the working condition for this work.

2.2 Numerical setup and model validation

A 3D geometrical model is established based on the PFI engine's specifications with the intake and exhaust manifolds, cylinder, and piston, as shown in Figure 3. 8 monitoring points (MP) are set evenly around the cylinder head to better detect knock pressure oscillation and end-gas condition, which are widely used in engine knock simulation researches[40,41]

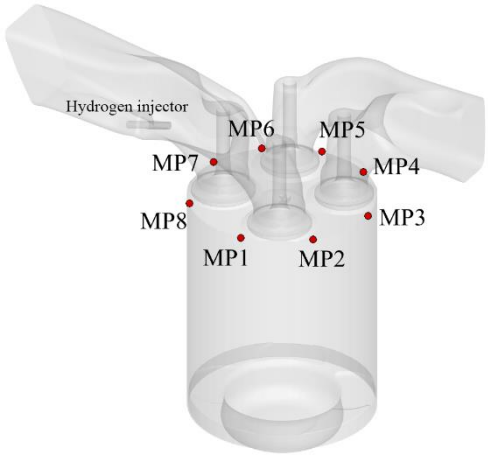


Figure 3 3D geometrical model with monitoring points

Commercial 3D CFD software CONVERGE 3.0 is applied in this research. The base grid size is set as 4 mm, and the grid refinements such as fixed embedding and Adapted Mesh Refinement (AMR) are used to control the magnitude of mesh to ensure simulation accuracy and shorten the calculation time. The refinement regions and different scales of refinement are shown in Table 3.

Table 3 Region and scale of fix embedding and AMR

Refinement region	Refine strategy/Scale
Combustion chamber	Fixed embedding/3
Spark plug	Fixed embedding/5

Injector exit	Fixed embedding/3
Intake/exhaust valve angle	Fixed embedding/4
Cylinder region	AMR/4
Inlet region (combustion)	AMR/4

The two-equation model RNG *k-ε* is used to simulate the mixing progress of hydrogen and air which has the advantages of high precision and low resource utilization[42,43], and it was widely applied to the engine knock research[20,44]. Han and Reitz's model is used to simulate heat transfer[45], which has more prediction accuracy of knock intensity[46], and is the most suitable heat transfer model for hydrogen engine simulation[47]. To accurately model the knock conditions, the detailed SAGE combustion model is selected with a detailed hydrogen chemical reaction mechanism of 19 elementary reactions [19,48,49], which can accurately simulate the combustion progress and flame propagation of hydrogen. The test conditions for validating the Maximum BTE operating point are shown in Table 4.

Table 4 Experimental condition for model validation.

Engine specification	Valve
Engine speed (rpm)	1400
Air fuel ratio (λ)	2.21
Duration of injection (°CA)	365~423
Ignition angle (°CA)	-8
Load (Brake mean effective pressure) (bar)	13
Intake valve open/close (°CA)	362/555
Exhaust valve open/close (°CA)	138/361

A negative crank angle denotes positions before top dead center (BTDC).

The result of the model validation is shown in Figure 4a. The simulation results match well with the experimental results within 3% error. In addition, base grid independence checking results are shown in Figure 4b. It can be seen that the results of the 3mm and 4mm base grid models are similar, however, there is a big difference between the 7 mm grid and the 3 mm grid. Taking into account simulation time, 4 mm is chosen as the magnitude of the base gird.

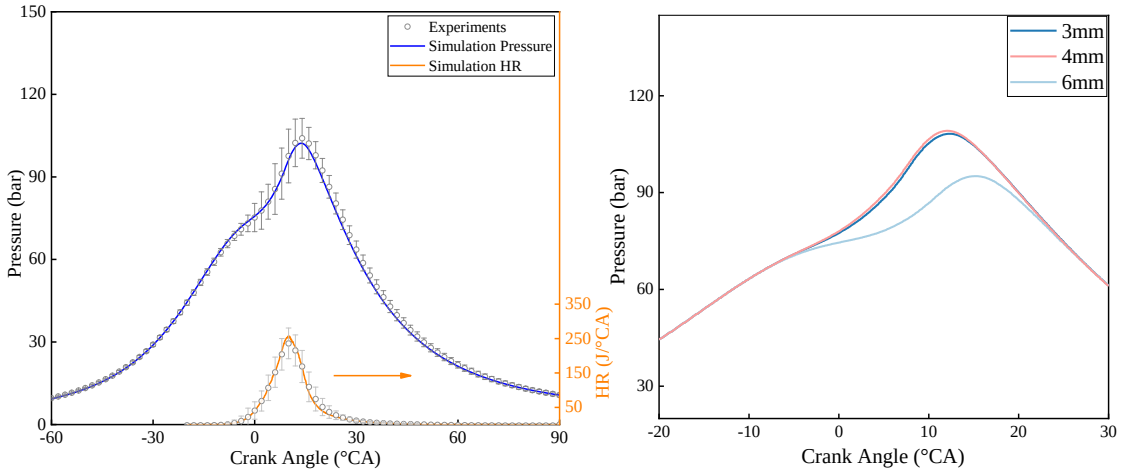


Figure 4 (a) Model validation with experiment; (b) Base grid selection

2.3 Multi-Cycle simulations

In order to reveal the backfire-induced knock phenomenon, a multi-cycle simulation is investigated. The multi-cycle simulation cycle orders are shown in Table 5. The first cycle is set as either a normal combustion cycle, named N1 or a backfire cycle named B1. B1 is based on N1, but backfire is induced by setting a hotspot. In a PFI hydrogen engine, a reasonable hypothesis about the backfire induced by a spark plug hotspot and exhaust gas is proposed by Dhyani et al.[50]. First of all, spark plug usually is the major hotspot of the engine at the high-load work condition because of the temperature, structure and space distribution, it is reasonable to set the spark plug as hotspot[51]. Secondly, previous research has demonstrated that spark plug hotspot is one of the most important causes of backfire, such as Khalid et al,[52], Gao et al.[53]. In addition, considering the wide flammable range and short quenching distance of hydrogen, the spark plug gap can provide the space for slow combustion of exhaust gas and lubricating oil particles, which is helpful for the occurrence of hotspots[54–56]. Therefore, in this research, the spark plug is chosen as the location of the hotspot. As shown in Table 5, following the N1 and B1 cycles, a second cycle is simulated, named the N2 and B2 cycles

(respectively a normal or a backfiring cycle). In addition, a cycle where the ignition angle is advanced to -13 °CA in order to compare the knock mechanism differences between backfire-induced knock and knock due to advanced ignition the – called the A2 cycle is also simulated.

Table 5 Baseline cycle settings.

Cycle Name	Previous Cycle	Ignition Angle (°CA)
N1	-	-8
B1	-	-8
N2	N1	-8
A2	N1	-13
B2	B1	-8

3 Results and discussions

3.1 Experimental and numerical comparison of backfire and super-knock cycles

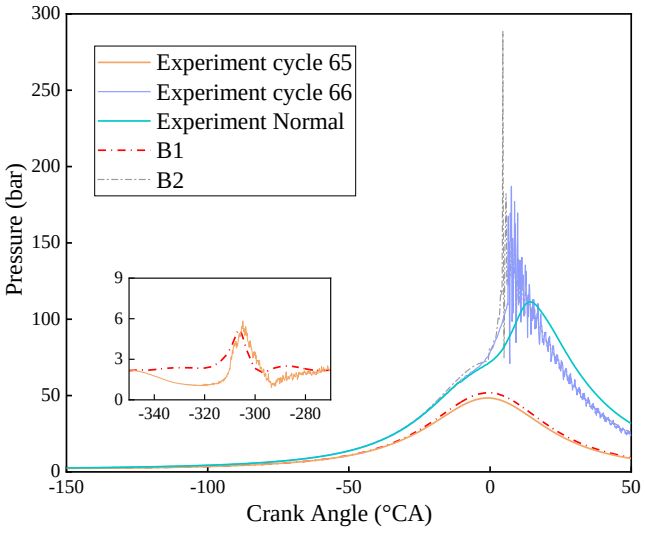


Figure 5 Experimental and numerical comparison of backfire and super-knock cycles

An experimental and numerical comparison of backfire and super-knock cycles are shown in Figure 5. In the intake stroke, the backfire phenomenon can be observed in both experimental cycle 65 and numerical cycle B1. The pressure oscillation's peak location and magnitude of cycle 65 and cycle N1 are similar, which are -309 °CA and 5.2 bar, respectively. With the piston compression, only a peak of 50 bar is achieved at the

TDC, no combustion pressure rise is detected due to backfire having consumed the hydrogen earlier in the cycles. The super-knock phenomenon is observed in the next cycles, which are experimental cycle 66 and numerical cycle B2, respectively. It is noticed that only the backfire phenomenon is induced by hotspot, the super-knock phenomenon is caused by the previous backfire cycle. The simulation study results are consistent with the experimental phenomena of backfire in the previous cycle and super-knock in the subsequent cycle.

3.2 Numerical investigation of abnormal combustion characteristics of backfire and super-knock

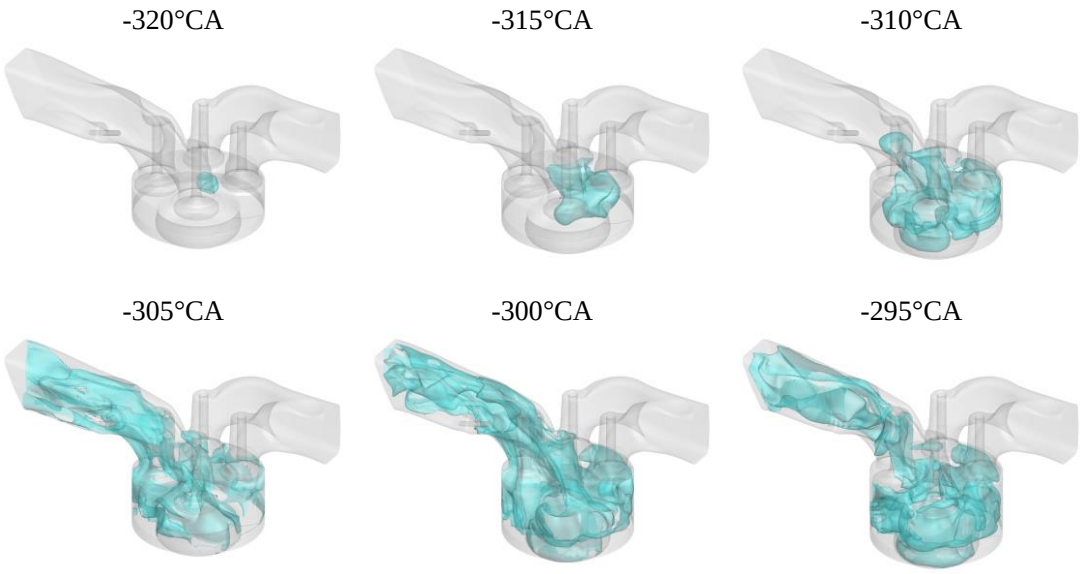


Figure 6 Development of flame of the backfire cycle

To explore the difference in the combustion process, the development of the flame front represented by the 1750K temperature iso-surface of a backfire cycle is shown in Figure 6. For the B1 cycle, the injection duration is -355~-297 °CA, and intake valve open/close events are -358°CA and -165°CA, respectively. Combustion is triggered by a hot spot near the spark plug at -320 °CA. The flame diffuses to the region under

the exhaust valve, following the flow-induced turbulence from -315 °CA to -310 °CA. It spreads into the manifold, accelerated by the rich mixture, and causes severe backfire (-305 °CA to -295° CA).

Figure 7 illustrates that the backfire flame reaches the intake valves at -315 °CA. Subsequently, the flame is divided into two flows, with the major one developing further in cylinder, mixing with the initial burning gases from the hotspot. The second flow extends into the intake manifold with a fast propagation velocity, causing intense combustion in the front of the manifold. Backfire continues till the end of hydrogen injection, burning up almost all of the injected hydrogen, without any combustion observed in the combustion cylinder after the compression stroke.

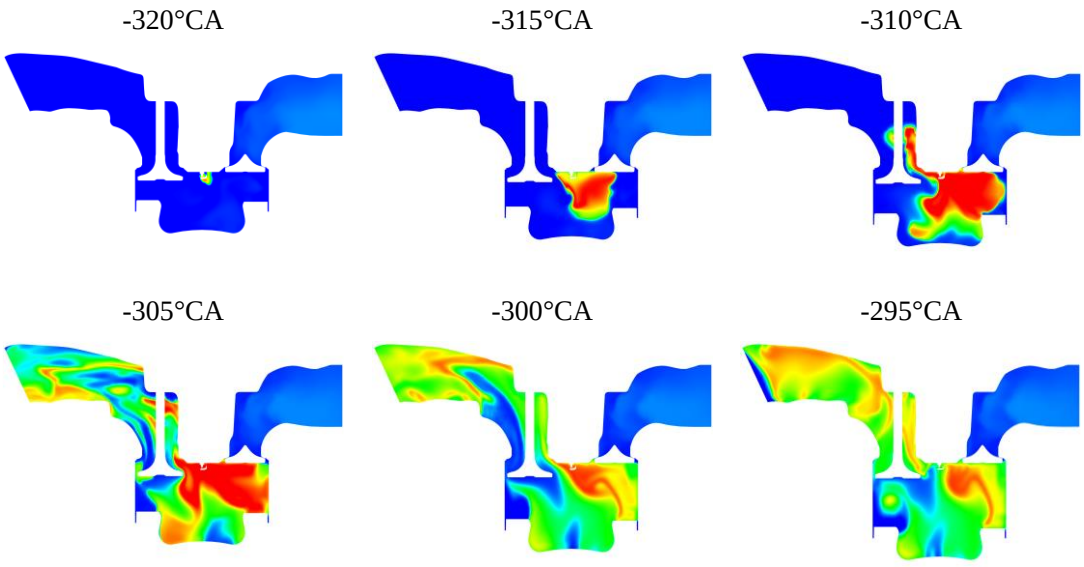


Figure 7 Temperature distribution of the backfire

Cylinder pressure of the second cycle is shown in Figure 8, where the peak of the normal cycle (N2) reaches 119 bar at 11.2 °CA. A slight amount of knock occurs in the advanced ignition cycle (A2), the cylinder pressure rises rapidly to 131.4 bar at 4.4 °CA, then keeps oscillating and reaches a maximum of 151 bar at 5.8 °CA. Notably, super-knock is detected in the cycle after backfire (B2). For the super-knock cycle (B2), there is a trend in the initial pressure increase similar to the A2 cycle. The pressure increases rapidly to 72.7

bar at -0.7 °CA (as in A2) and then a sharp pressure peak suddenly occurs at 4.6°CA, with a maximum pressure of 288.6 bar reached and substantial oscillations until the combustion ends.

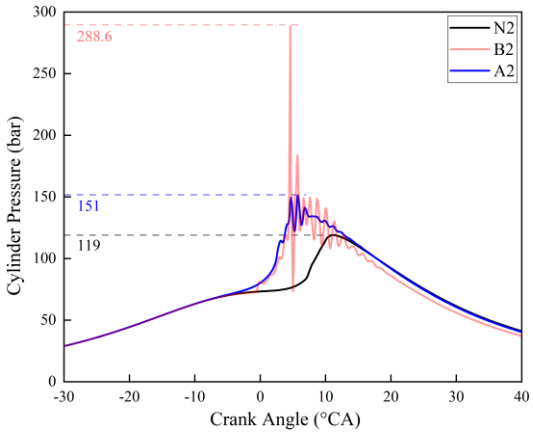


Figure 8 Cylinder Pressure comparison of the second cycles showing a backfire cycle (B2), normal cycle (N2), and a normal knocking cycle (A2)

Further exploring the knock characteristics of knock cycles, the knock pressure oscillation is illustrated by Bandpass filtering (the frequency of Bandpass is 3k~25kHz) in Figure 9. In terms of the A2 cycle, the knock onset crank angle (KOCA) is 2.4 °CA, and the Maximum Amplitude of Pressure Oscillation (MAPO) is 19.6 bar. In contrast, the KOCA of the B2 cycle is advanced to -0.6 °CA and the MAPO reaches 134.7 bar. From the difference of MAPO, the knock intensity of A2 and B2 cycles can be differentiated into normal knock and super-knock.

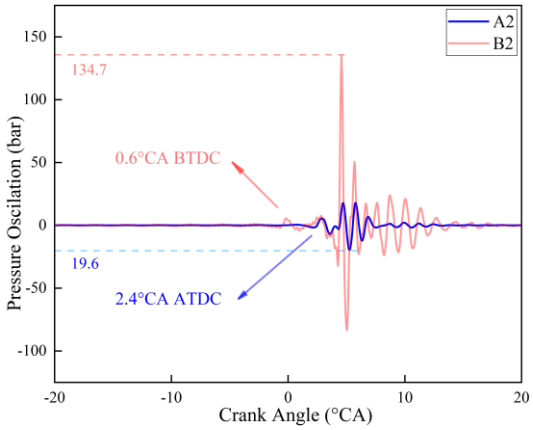


Figure 9 Cylinder Pressure Oscillation of two knock cycles normal knock (A2) and super-knock (B2)

3.3 Comparison of the cylinder mixture distribution and in-flow before the knock occurs

In order to investigate the mechanisms of super-knock occurrence in the B2 cycle, excess air-fuel ratio (λ), temperature, and TKE distribution at -20 °CA before the knock occurs are compared between the B2 and N2 cycles. A significant difference in the in-cylinder hydrogen distribution between the two cycles is shown in Figure 10. The hydrogen distribution is uneven for the B2 cycle, with ultra-lean mixtures (λ=2.9) near the spark plug, and relatively rich mixtures (λ=1.2) clustered in the bowl of the combustion chamber. In contrast, a homogeneous distribution is observed in the N2 cycle, and the local λ near the spark plug reaches 2.3, which is very close to the global λ of 2.21.

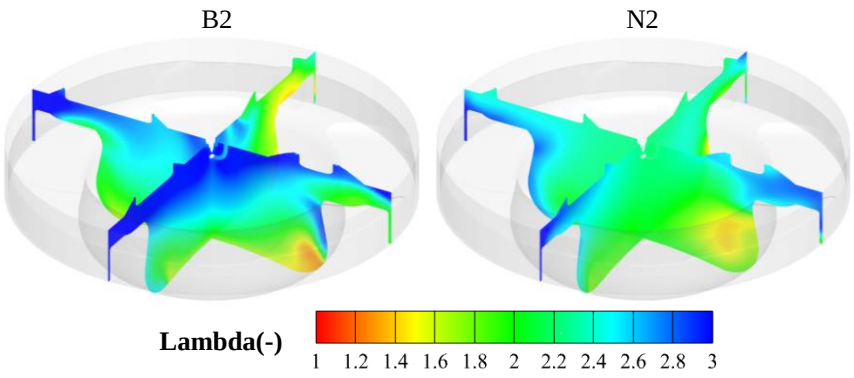


Figure 10 In cylinder λ for the B2 and N2 cycles at -20 °CA

As shown in Figure 11, TKE approaches zero near the chamber wall, and high TKE regions of 20 m^2/s^2 are located near the cylinder head and at the bottom of the piston bowl for the B2 cycle. In comparison, the high TKE region of the N2 cycle is concentrated at the bottom of chamber, with considerable turbulence flow near the cylinder wall. Consequently, low-flow near the walls reduces the wall heat transfer process and leads to elevated temperatures during the B2 cycle.

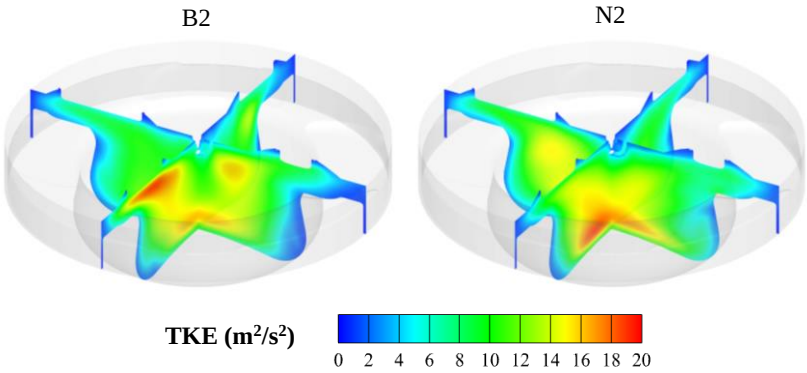


Figure 11 In cylinder TKE for the B2 and N2 cycles at -20 °CA

Figure 12, presents the in-cylinder temperature for the B2 and N2 cycles. It can be seen that the temperature transition is smooth in the N2 cycle, with a lower temperature of 850 K near the cylinder head and a higher temperature of 915 K at the bottom of the cylinder. Meanwhile, the B2 cycle shows a mostly similar temperature distribution but with a higher temperature zone of 930 K corresponding to the rich region in Figure 11.

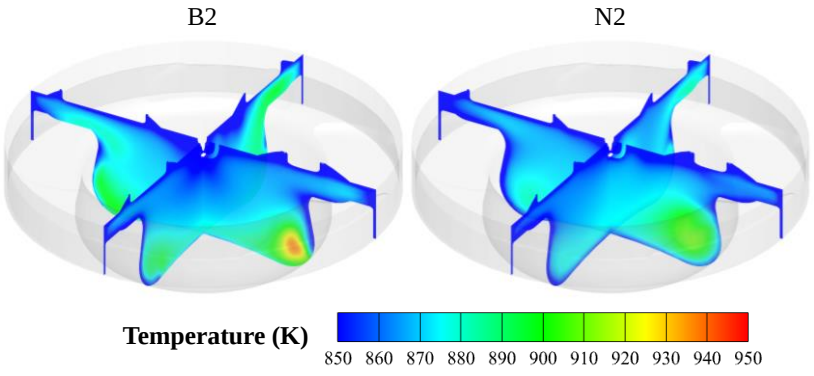


Figure 12 In cylinder temperature for the B2 and N2 cycles at -20°CA

As shown in Figure 13, an analysis of the flow field during the mixing progress is conducted. Streamlines represent the in-flow direction and distribution, where the color of the lines indicates λ of passing through regions. In addition, rich hydrogen regions are also represented by the iso-surfaces of λ at λ = 1.2 to 1.4. Relatively rich regions of λ<1.4 at -60 °CA exist in both cycles, however this is limited in the N2 cycle.

In contrast, rich mixtures of λ=1.2 are distributed at the bottom of the chamber near the cylinder wall in the B2 cycle which persist right up to -20 °CA.

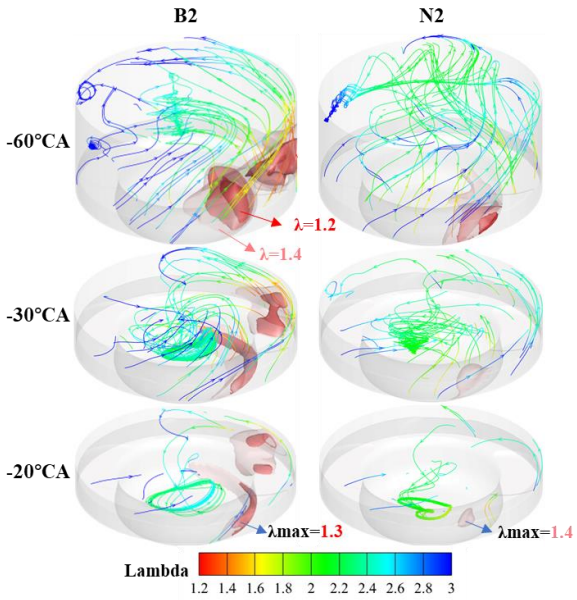


Figure 13 In-cylinder flow and λ distribution for the B2 and N2 cycles

Figure 14 shows that the internal flow direction of the B2 cycle is counterclockwise and mainly clusters in the center of the chamber, while no streamlines cross the rich regions at the bottom. In contrast, some streamlines pass through the low λ region in the N2 cycle, facilitating the mixing of hydrogen with the air and leading to a homogeneous mixture before the combustion. For the B2 cycle, vortex flows still concentrate in the center of the chamber at -20 °CA, resulting in a higher hydrogen accumulation in this region compared to the N2 cycle, accelerating the occurrence of super-knock.

In summary, inadequate mixing within the cylinder increases the tendency for knocking combustion in these cycles. Compared to the N2 cycle, a lower hydrogen concentration near the spark plug of the B2 cycle, results in a slower flame propagation velocity, leaving sufficient time for the end-gas autoignition. Increasing intake gas temperature and local temperature of cylinder walls also intensifies the tendency of knocking

combustion. This leads to backfire-induced super-knock, which is accelerated by these initial physical conditions, and detailed mechanisms are studied in the following section.

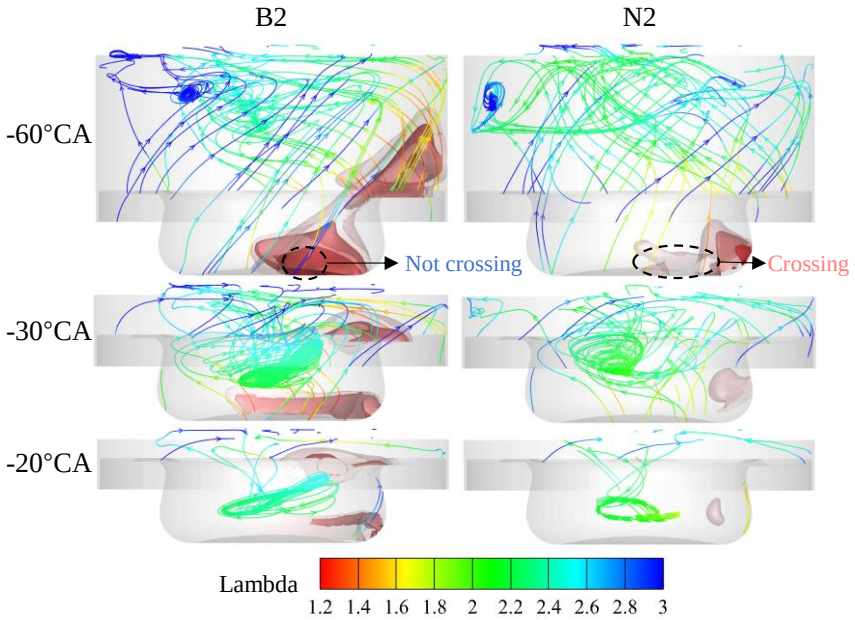


Figure 14 The relationship between rich regions and cylinder flow for the B2 and N2 cycles

3.4 Comparison of mechanism between the super-knock and the normal knock

The knock flame propagation process of super-knock in the B2 cycle is shown in Figure 15, where the flame front is identified by the 1750 K temperature iso-surface. It is seen that the initial ignition flame develops slowly around the spark plug at -1.5 °CA. Subsequently, autoignition occurs in the unburned region near the cylinder wall, corresponding to the first cylinder pressure oscillation at -1.3 °CA in Figure 9. Compared to the initial flame core, the autoignition flame spreads rapidly, causing the first cylinder pressure oscillation. The first autoignition flame develops along the bottom edge of the chamber and merges with the initial flame at 3.5 °CA. A second autoignition is detected in the unburned region at 3.6 °CA. Subsequently, the unburned region burns rapidly due to the second autoignition, causing a sharp cylinder pressure increase.

Therefore, super-knock is attributed to the two autoignitions occurring in the same cycle, and further studies illustrate different effects of two autoignitions on the total combustion progress. To further illustrate the mechanism of the differences, mass fractions of radicals with temperature change trace paths are discussed next.

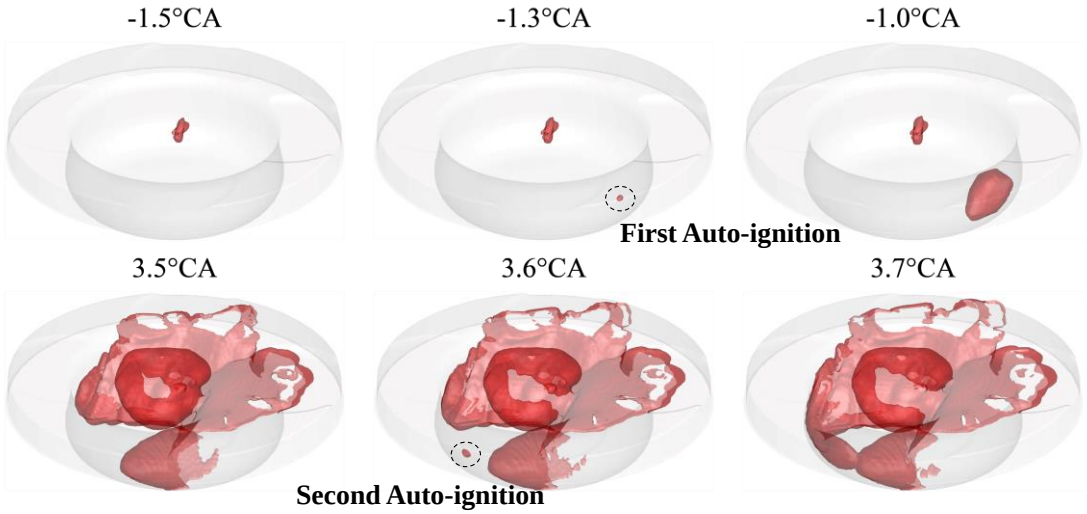
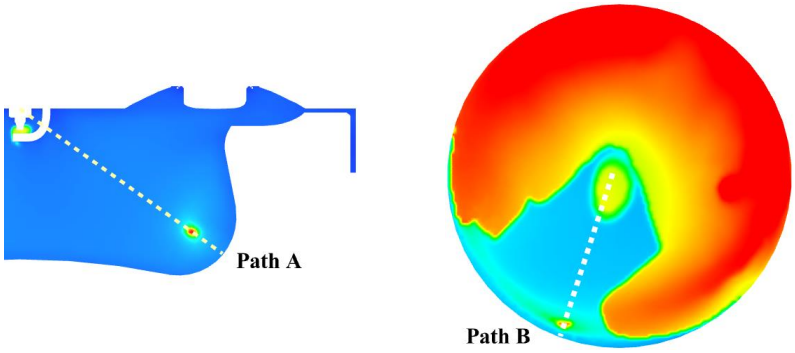


Figure 15 Knock flame propagation in the B2 cycle



(a) (b)

Figure 16 Scheme of Paths in the B2 cycle: (a) Path A during -1.4 °CA to -1.2 °CA (the first autoignition); (b) Path B during 3.5 °CA to 3.7 °CA (the second autoignition)

Figure 16 shows the location of a trace path on a slice where autoignition occurs. Path A and Path B are set starting from the center of the upper combustion chamber surface and passing through the first and second autoignition kernels, respectively. Here the distance represents the length of the path where the center of the

combustion chamber is defined as 0 mm. Changes in mass fractions of radicals and temperature along the paths are depicted in Figure 17 and Figure 18.

As illustrated in Figure 17, autoignition occurs at the point 32.7 mm along Path A at -1.3 °CA. Before the autoignition happens, there is a significant increase in the mass fraction of HO_2 and H_2O_2 along Path A, with a maximum of 5.4×10^{-4} and 2×10^{-3} at -1.4 °CA. Meanwhile, the peak temperature increases to 1232.9 K. HO_2 and H_2O_2 radicals are consumed rapidly, and the mass fraction of the OH radical increases to 2.67×10^{-3} with the temperature rising to 2357.6 K at -1.3 °CA when autoignition occurs. Subsequently, at -1.2 °CA, the temperature rises to 2471 K with complete consumption of the HO_2 and H_2O_2. Meanwhile, the autoignition kernel begins to spread.

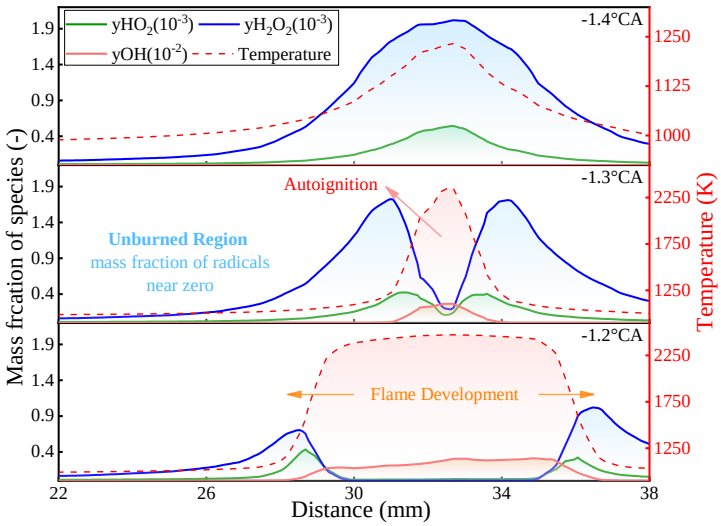


Figure 17 Mass fraction distribution of species along the Path A during -1.4 to -1.2 °CA

As shown in Figure 18, another autoignition occurs at 3.6 °CA, 32.8mm along Path B. At 3.5 °CA, the mass fractions of HO_2 and H_2O_2 are 4×10^{-4} and 1.18×10^{-3}, respectively. The HO_2 and H_2O_2 radicals are completely consumed with the temperature rising from 1251 K to 2209 K, and the mass fraction of OH radical increases to 4.1×10^{-3} at 3.6 °CA.

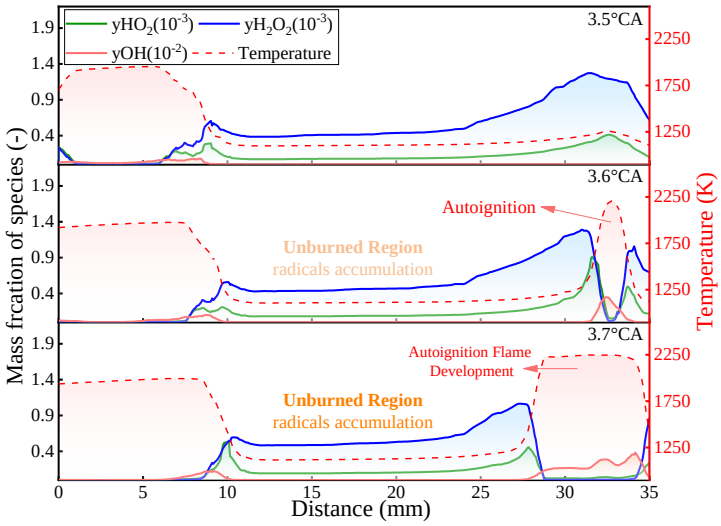


Figure 18 Mass fraction distribution of species along Path B during 3.5 to 3.7 °CA

Hence, the mechanism of autoignition can be explained by elementary reactions[12]. At the beginning, initial excitation reaction (1) and low-temperature reaction (2) predominate. The mass fraction of the HO_2 radical keeps rising, and since the temperature of the cylinder is insufficient, reactions (3) and (4) become the main pathways for the H_2O_2 radical formation.

$$H_2 + O_2 = HO_2 + H \quad (1)$$

$$H + O_2 + M = HO_2 + M \quad (2)$$

$$HO_2 + H_2 = H_2O_2 + H \quad (3)$$

$$HO_2 + HO_2 = H_2O_2 + O_2 \quad (4)$$

As the temperature and mass fractions of radicals increase, the dominance of chain propagation reactions (5), (6), and (7) initiates, and speed of these reactions leads to autoignition at the location of substantial radical accumulation.

$$HO_2 + H = OH + OH \quad (5)$$

$$HO_2 + O = OH + O_2 \quad (6)$$

$$H_2O_2 + M = OH + OH + M \quad (7)$$

The reasons for different combustion states caused by two instances of autoignition can be obtained by variations in radicals' mass fractions and temperature along two pathways. At the first autoignition, despite the spontaneous flame kernel generated, only the surrounding locations exhibit higher temperatures. As a result, these peripheral positions produce low mass fractions of radicals, causing the flame to propagate at a slow speed. Consequently, it impedes the development of intense combustion and prevents the occurrence of substantial knock. In terms of the second autoignition, it can be observed that the mass fractions of radicals at unburned region are higher. For example, at 15mm along Path B, the mass fractions of HO_2 and H_2O_2 are 1×10^{-4} and 5.3×10^{-4}, respectively. This is because as heat diffuses, it subsequently raises the temperature in the unburned regions, promoting the onset of low-temperature reactions. During the second autoignition, the temperature inside the cylinder is higher, facilitating extensive low-temperature reactions in the unburned areas. This leads to a substantial overall mass fractions of radicals in the cylinder. Meanwhile, the chain propagation reactions are significantly accelerated by heightened mass fractions of radicals, resulting in a rapid spread of combustion flame after autoignition occurs. Consequently, the swift development of the flame induces a sharp increase in pressure in the unburned region, causing pressure wave fluctuations in the cylinder - the super-knock phenomena.

The flame development of the normal knock A2 cycle is illustrated in Figure 19. At 3.6 °CA, the flame has essentially diffused into most areas of the cylinder, with only the space near the combustion chamber wall remaining unburned. Between 3.6 and 3.7 °CA, due to a reduction in hydrogen concentration, the flame develops slowly. At 3.8 °CA, autoignition of end-gas occurs suddenly in the unburned region and the flame propagates rapidly in the unburned area and extending upwards at 3.9 °CA.

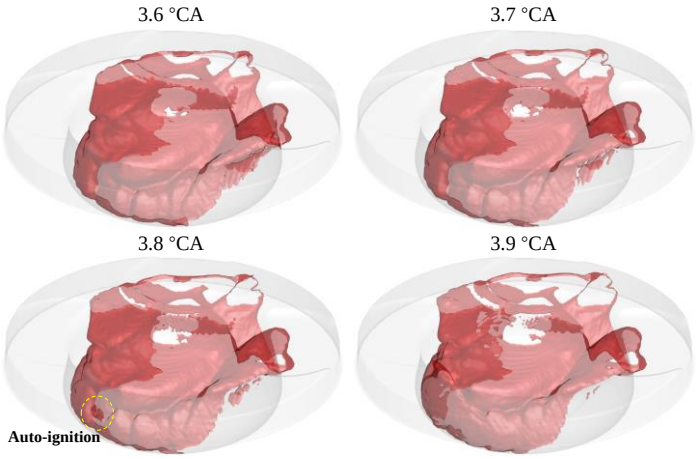


Figure 19 Flame development of knock in the A2 cycle

Path C of the flame autoignition zone is shown in Figure 20. Figure 21 presents the variation of radicals' mass fractions and temperature along Path C during normal knock. At 3.6 °CA, the overall temperature along Path C exceeds 1150K, and the radicals' mass fractions are notably high. The mass fractions of HO_2 and H_2O_2 are primarily around 2.1×10^{-4} and 9.1×10^{-4}, respectively with a slightly lower magnitude on the right-hand side of the path. From 3.6 °CA to 3.7 °CA, the overall temperature shows an increasing trend influenced by the propagation of flame temperature. At some points, such as 6.5 mm and 9 mm, the temperature rises slightly more, reaching approximately 1250 K. Mass fractions of HO_2 and H_2O_2 radicals along the entire path also increase to around 4×10^{-4} and 1.2×10^{-3}, respectively. Subsequently, at 3.8 °CA, autoignition occurs in the regions where the temperature had increased earlier, specifically at 6.5 mm and 9 mm. Combustion at 1.3 mm on the left side occurs due to the propagation of the initial flame.

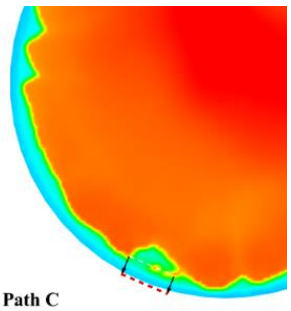


Figure 20 The location of Path C during 3.6 to 3.8 °CA ATDC

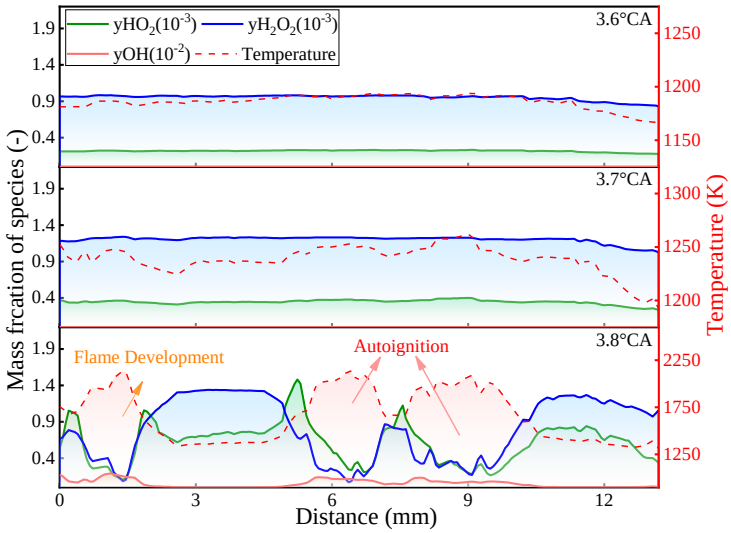


Figure 21 Mass fraction distribution of species along the Path C during 3.6 to 3.8 °CA

It is noteworthy that, at the autoignition location, patterns of the A2 cycle are similar to the B2 cycle, such as rapid consumption of HO_2 and H_2O_2 radicals and generating OH radicals. However, compared to the flame temperature of 2209 K in the B2 cycle, it is apparent that flame temperature is lower at 2086 K. The temperature, in turn, influences the rate of chain propagation reactions, resulting in an overall reaction rate lower than that of the B2 cycle. The comparison between the two knock cycles reveals the reasons for the difference in knock intensity and is explained as follows.

Firstly, through the comparison of the first and second autoignition events in the B2 cycle, it is evident that the development of autoignition flames requires a significant accumulation of radicals along the flame propagation path. If the overall mass fraction of radicals is low, it cannot support the rapid progression of chain reactions. Therefore, separate autoignition provides sufficient radicals for the development of the second autoignition.

Secondly, the size of the unburned region is found to play a crucial role when comparing the second autoignition of the B2 cycle with the knock phenomenon of the A2 cycle. In both cycles, free radicals exist sufficiently in the unburned region before knock occurs. However, the unburned region of the super-knock

cycle is much larger compared to the normal knock cycle. It supports the rapid development of autoignition flames due to higher remaining hydrogen concentration and provides space for the conduction of knock pressure waves. In the A2 cycle, the smaller unburned region results in a lower effect on the magnitude of radicals' mass, impeding the faster development of the flame. Besides, part of the radicals intended for the rapid spread of autoignition flames are consumed by the diffusion flame. These factors weaken the development speed of the autoignition flame, consequently resulting in lower knock intensity.

Finally, corresponding methods to suppress knock can be proposed after the study of the mechanism. Firstly, it is seen that mixture uniformity and local hydrogen concentration significantly impact the knock occurrence of the large-bore PFI hydrogen engines. Secondly, the present study indicates that temperature distribution plays a critical role in autoignition. Therefore, knock can be suppressed by adjusting intake pressure, using EGR, and appropriately reducing intake temperature. Furthermore, since backfire can induce super-knock, reducing hot spots by cooling spark plugs and reducing valve overlap can also reduce the super-knock tendency.

4 Conclusion

In this paper, a knock investigation based on a 5.13 L PFI hydrogen engine is carried out. The phenomena of backfire, backfire-induced super-knock, and normal knock induced by advanced ignition are discussed and analyzed. The mechanism of super-knock induced by backfire in hydrogen engine is first been proposed and this study contributes to hydrogen energy application by providing insights into avoiding super-knock, thereby achieving stable combustion with higher engine performance in hydrogen engines. The main conclusions are:

(1) Backfire is induced by setting a hotspot, and fresh hydrogen-air mixture is ignited by the hotspot which is located at the spark plug. Most of the hydrogen is consumed by the backfire combustion, resulting in no combustion phenomenon in the combustion cylinder at TDC during the rest of the cycle.

(2) Inadequate mixing within the cylinder intensifies the tendency for backfire-induced knock combustion. Both local rich regions of lambda=1.2, and high local temperature of 915K significantly heighten the likelihood of autoignition formation and consequently, intensify the tendency of knock combustion.

(3) HO_2 and H_2O_2 radicals play important roles in the occurrence of autoignition. For low-temperature reactions, radicals accumulate when the temperature reaches 970 K and autoignition takes place at the critical temperature of 1250 K.

(4) The quantity of accumulated radicals during autoignition influences the temperature of the autoignition flame. The temperature of the first and second autoignitions in B2 cycle are 2357.6 K and 2209 K, with corresponding mass fractions of HO_2/H_2O_2 of $5.4\times10^{-4}/2\times10^{-3}$ and $4\times10^{-4}/1.18\times10^{-3}$, respectively.

(5) The onset of knock is a consequence of the combined effects of radicals' accumulation and the size of the unburned region. For the first autoignition in the B2 cycle, despite the spontaneous flame kernel generated, the surrounding locations exhibit higher temperature and much lower mass fraction of radicals. In contrast, the mass fractions of HO_2/H_2O_2 in the second autoignition's unburned region are $1\times10^{-4}/5.3\times10^{-4}$. Both autoignition points meet the requirements of the unburned zone size, but the difference in the content of radicals in the unburned zone leads to different knocking phenomena.

(6) The unburned region size also determines the knock intensity. In the A2 cycle, the smaller unburned region results in an overall lower magnitude of radicals' mass compared with the B2 cycle, the mass fraction of HO_2/H_2O_2 are 4×10^{-4} and 1.2×10^{-3}, respectively. In addition, because of the autoignition

location close to the diffusion flame, some of the radicals which could be used in the rapid spread of autoignition flames are consumed by the diffusion flame, consequently resulting in lower knock intensity.

Acknowledgements

This study was supported by the China Postdoctoral Science Foundation (2023M730238); Young Elite Scientists Sponsorship Program by CAST (2023QNRC001); National Natural Science Foundation of China (Grant No.:52206228); Technology Integration Validation of Marine Low Carbon & Zero Carbon Low Speed Engine; Natural Science Foundation of Chongqing Municipality (CSTB2023NSCQ-MSX0399)

References:

[1] Algayyim SJM, Saleh K, Wandel AP, Fattah IMR, Yusaf T, Alrazen HA. Influence of natural gas and hydrogen properties on internal combustion engine performance, combustion, and emissions: A review. Fuel 2024;362:130844. https://doi.org/10.1016/j.fuel.2023.130844.

[2] Xie F, Liang Z, Lai K, Liu Y, Wang Z, Li X. Influence of operating parameters on hydrogen DISI engine at injection pressure-drop by experimental investigation and Taguchi method. Fuel 2024;362:130840. https://doi.org/10.1016/j.fuel.2023.130840.

[3] Ji C, Wu S, Yi Y, Yang J, Wang H, Meng H, et al. Effects of hydrogen injection strategies on the flow field and combustion characteristics in a hydrogen-fueled rotary engine with the swirl chamber. Fuel 2024;364:130951. https://doi.org/10.1016/j.fuel.2024.130951.

[4] El-Adawy M, Nemitallah MA, Abdelhafez A. Towards sustainable hydrogen and ammonia internal combustion engines: Challenges and opportunities. Fuel 2024;364:131090. https://doi.org/10.1016/j.fuel.2024.131090.

[5] Huang Z, Yuan S, Wei H, Zhong L, Hu Z, Liu Z, et al. Effects of hydrogen injection timing and injection pressure on mixture formation and combustion characteristics of a hydrogen direct injection engine. Fuel 2024;363:130966. https://doi.org/10.1016/j.fuel.2024.130966.

[6] Golisano R, Scalabrini S, Sacco N. System Optimization in a State-of-the-Art V8 6.6l Hydrogen Engine, 2023.

[7] Tsujimura T, Suzuki Y. Development of a large-sized direct injection hydrogen engine for a stationary power generator. Prod Storage Valorization Hydrog Energy PSVHE 2019;44:11355–69. https://doi.org/10.1016/j.ijhydene.2018.09.178.

458 [8] Fischer M, Sterlepper S, Pischinger S, Seibel J, Kramer U, Lorenz T. Operation principles for
459 hydrogen spark ignited direct injection engines for passenger car applications. Int J Hydrog Energy
460 2022;47:5638–49.
461 [9] Bao L, Sun B, Luo Q, Li J, Qian D, Ma H, et al. Development of a turbocharged direct-injection
462 hydrogen engine to achieve clean, efficient, and high-power performance. Fuel 2022;324:124713.
463 https://doi.org/10.1016/j.fuel.2022.124713.
464 [10] Kalghatgi GT. Developments in internal combustion engines and implications for combustion
465 science and future transport fuels. Proc Combust Inst 2015;35:101–15.
466 https://doi.org/10.1016/j.proci.2014.10.002.
467 [11] Ceschini L, Morri A, Balducci E, Cavina N, Rojo N, Calogero L, et al. Experimental observations
468 of engine piston damage induced by knocking combustion. Mater Des 2017;114:312–25.
469 https://doi.org/10.1016/j.matdes.2016.11.015.
470 [12] Szwaja S, Bhandary K, Naber J. Comparisons of hydrogen and gasoline combustion knock in a
471 spark ignition engine. Int J Hydrog Energy 2007;32:5076–87.
472 https://doi.org/10.1016/j.ijhydene.2007.07.063.
473 [13] Wang L, Yang Z, Huang Y, Liu D, Duan J, Guo S, et al. The effect of hydrogen injection parameters
474 on the quality of hydrogen–air mixture formation for a PFI hydrogen internal combustion engine. Int J
475 Hydrog Energy 2017;42:23832–45. https://doi.org/10.1016/j.ijhydene.2017.04.086.
476 [14] Reichel TG, Paschereit CO. Interaction mechanisms of fuel momentum with flashback limits in
477 lean-premixed combustion of hydrogen. Int J Hydrog Energy 2017;42:4518–29.
478 https://doi.org/10.1016/j.ijhydene.2016.11.018.

[15] Lai F, Sun B, Wang X, Zhang D, Luo Q, Bao L. Research on the inducing factors and characteristics of knock combustion in a DI hydrogen internal combustion engine in the process of improving performance and thermal efficiency. Int J Hydrog Energy 2023;48:7488–98. https://doi.org/10.1016/j.ijhydene.2022.11.091.

[16] Hu Z, Ma W, Ma J, Zhou L, Wei H, Wei H, et al. Experimental Research on Performance Development of Direct Injection Hydrogen Internal Combustion Engine with High Injection Pressure. SAE Int J Engines 2023;16.

[17] Meng H, Ji C, Yang J, Chang K, Xin G, Wang S. A knock study of hydrogen-fueled Wankel rotary engine. Fuel 2022;321:124121. https://doi.org/10.1016/j.fuel.2022.124121.

[18] Wang K, Zhang Z, Sun B, Zhang S, Lai F, Ma N, et al. Experimental investigation of the working boundary limited by abnormal combustion and the combustion characteristics of a turbocharged direct injection hydrogen engine. Energy Convers Manag 2024;299:117861. https://doi.org/10.1016/j.enconman.2023.117861.

[19] Li Y, Gao W, Zhang P, Fu Z, Cao X. Influence of the equivalence ratio on the knock and performance of a hydrogen direct injection internal combustion engine under different compression ratios. Int J Hydrog Energy 2021;46:11982–93. https://doi.org/10.1016/j.ijhydene.2021.01.031.

[20] Ye Y, Gao W, Li Y, Zhang P, Cao X. Numerical study of the effect of injection timing on the knock combustion in a direct-injection hydrogen engine. Int J Hydrog Energy 2020;45:27904–19. https://doi.org/10.1016/j.ijhydene.2020.07.117.

[21] Li Y, Gao W, Li Y, Fu Z, Zou J. Numerical investigation on combustion and knock formation mechanism of hydrogen direct injection engine. Fuel 2022;316:123302. https://doi.org/10.1016/j.fuel.2022.123302.

[22] Yu H, Chen Z. End-gas autoignition and detonation development in a closed chamber. Combust Flame 2015;162:4102–11. https://doi.org/10.1016/j.combustflame.2015.08.018.

[23] Hong C, Xin G, Xu S, Cai J, Su F, Wang S, et al. An experimental study of knock in a DI hydrogen engine: The synergistic effects of the deep Miller cycle and oxygen-enriched atmosphere. Energy Convers Manag 2024;306:118269. https://doi.org/10.1016/j.enconman.2024.118269.

[24] Kufferath A, Schünemann E, Krüger M, Krüger M, Jianye S, Eichlseder H, et al. H2 ICE Powertrains for future on-road mobility, 2021, p. 29–30.

[25] Winklhofer E, Jocham B, Philipp H, Kapus P, Leitner D, Heindl R, et al. Hydrogen ICE Combustion Challenges. SAE Technical Paper; 2023.

[26] Maio G, Boberic A, Giarracca L, Aubagnac-Karkar D, Colin O, Duffour F, et al. Experimental and numerical investigation of a direct injection spark ignition hydrogen engine for heavy-duty applications. Int J Hydrog Energy 2022;47:29069–84. https://doi.org/10.1016/j.ijhydene.2022.06.184.

[27] Verhelst S, Wallner T. Hydrogen-fueled internal combustion engines. Prog Energy Combust Sci 2009;35:490–527. https://doi.org/10.1016/j.pecs.2009.08.001.

[28] Liang Z, Xie F, Guo Z, Wang Z, Dou H, Wang B, et al. Optimization and prediction of a novel preignition in hydrogen direct injection engines through experimentation and the Random forest algorithms. Energy Convers Manag 2024;313:118602. https://doi.org/10.1016/j.enconman.2024.118602.

[29] Yang Z, Wu J, Yun H, Zhang H, Xu J. Diagnosis and control of abnormal combustion of hydrogen internal combustion engine based on the hydrogen injection parameters. Int J Hydrog Energy 2022;47:15887–95. https://doi.org/10.1016/j.ijhydene.2022.03.031.

[30] Diéguez PM, Urroz JC, Sáinz D, Machin J, Arana M, Gandía LM. Characterization of combustion anomalies in a hydrogen-fueled 1.4 L commercial spark-ignition engine by means of in-cylinder pressure, block-engine vibration, and acoustic measurements. Energy Convers Manag 2018;172:67–80. https://doi.org/10.1016/j.enconman.2018.06.115.

[31] Duan J, Liu F, Sun B. Backfire control and power enhancement of a hydrogen internal combustion engine. Int J Hydrog Energy 2014;39:4581–9. https://doi.org/10.1016/j.ijhydene.2013.12.175.

[32] Gong C, Li Z, Yi L, Sun J, Liu F. Comparative analysis of various combustion phase control methods in a lean-burn H2/methanol fuel dual-injection engine. Fuel 2020;262:116592. https://doi.org/10.1016/j.fuel.2019.116592.

[33] Salvi BL, Subramanian KA. Experimental investigation on effects of compression ratio and exhaust gas recirculation on backfire, performance and emission characteristics in a hydrogen fuelled spark ignition engine. Int J Hydrog Energy 2016;41:5842–55. https://doi.org/10.1016/j.ijhydene.2016.02.026.

[34] Menaa A, Lounici MS, Amrouche F, Loubar K, Kessal M. CFD analysis of hydrogen injection pressure and valve profile law effects on backfire and pre-ignition phenomena in hydrogen-diesel dual fuel engine. Int J Hydrog Energy 2019;44:9408–22. https://doi.org/10.1016/j.ijhydene.2019.02.123.

[35] Jiang L, Vanier J, Yilmaz H, Stefanopoulou A. Parameterization and Simulation for a Turbocharged Spark Ignition Direct Injection Engine with Variable Valve Timing, 2009, p. 2009-01–0680. https://doi.org/10.4271/2009-01-0680.

[36] Luo Q, Sun B. Inducing factors and frequency of combustion knock in hydrogen internal combustion engines. Int J Hydrog Energy 2016;41:16296–305. https://doi.org/10.1016/j.ijhydene.2016.05.257.

[37] Dhyani V, Subramanian KA. Experimental investigation on effects of knocking on backfire and its control in a hydrogen fueled spark ignition engine. Int J Hydrog Energy 2018;43:7169–78. https://doi.org/10.1016/j.ijhydene.2018.02.125.

[38] Marwaha A, Subramanian KA. Experimental investigation on backfire occurrence, duration and termination in a hydrogen-fueled automotive spark ignition engine. Process Saf Environ Prot 2024;189:322–42. https://doi.org/10.1016/j.psep.2024.06.091.

[39] Lai F, Sun B, Xiao G, Luo Q, Bao L. Research on optimizing turbo-matching of a large-displacement PFI hydrogen engine to achieve high-power performance. Int J Hydrog Energy 2023;48:38508–20. https://doi.org/10.1016/j.ijhydene.2023.06.104.

[40] Feng H, Suo X, Xiao S, Chen X, Zhang Z, Gao N, et al. Numerical simulation on the effects of n-butanol combined with intake dilution on engine knock. Energy 2023;271:126918. https://doi.org/10.1016/j.energy.2023.126918.

[41] Huang H, Xing K, Ning D, Guo X, Wang Y. Quantitative analysis of the relationship between charge motion and knocking combustion in spark-ignition natural-gas engines under critical knocking conditions. Fuel 2024;371:132060. https://doi.org/10.1016/j.fuel.2024.132060.

[42] Li Y, Gao W, Zhang P, Ye Y, Wei Z. Effects study of injection strategies on hydrogen-air formation and performance of hydrogen direct injection internal combustion engine. Int J Hydrog Energy 2019;44:26000–11. https://doi.org/10.1016/j.ijhydene.2019.08.055.

[43] Addepalli SK, Pei Y, Zhang Y, Scarcelli R. Multi-dimensional modeling of mixture preparation in a direct injection engine fueled with gaseous hydrogen. Int J Hydrog Energy 2022;47:29085–101. https://doi.org/10.1016/j.ijhydene.2022.06.182.

[44] Gong Z, Feng L, Wang Z. Experimental and numerical study of the effect of injection strategy and intake valve lift on super-knock and engine performance in a boosted GDI engine. Fuel 2019;249:309–25. https://doi.org/10.1016/j.fuel.2019.03.005.

[45] Han Z, Reitz RD. A temperature wall function formulation for variable-density turbulent flows with application to engine convective heat transfer modeling. Int J Heat Mass Transf 1997;40:613–25. https://doi.org/10.1016/0017-9310(96)00117-2.

[46] Liu S, Qi Y, Lin Z, Liu W, Lu G, Wang B, et al. A wall heat transfer model and a skeletal reaction mechanism of iso-octane for CFD simulatiaon of gasoline engines. Energy Convers Manag 2023;298:117784. https://doi.org/10.1016/j.enconman.2023.117784.

[47] Dou X, Yosri M, Talei M, Yang Y. Impact of wall heat transfer modelling in large-eddy simulation of hydrogen knocking combustion. Int J Hydrog Energy 2024;62:405–17. https://doi.org/10.1016/j.ijhydene.2024.03.076.

[48] Li J, Zhao Z, Kazakov A, Dryer FL. An updated comprehensive kinetic model of hydrogen combustion. Int J Chem Kinet 2004;36:566–75. https://doi.org/10.1002/kin.20026.

578 [49] Li Y, Gao W, Li Y, Fu Z, Zou J. Numerical investigation on combustion and knock formation
579 mechanism of hydrogen direct injection engine. Fuel 2022;316:123302.
580 https://doi.org/10.1016/j.fuel.2022.123302.
581 [50] Dhyani V, Subramanian KA. Fundamental characterization of backfire in a hydrogen fuelled spark
582 ignition engine using CFD and experiments. Int J Hydrog Energy 2019;44:32254–70.
583 https://doi.org/10.1016/j.ijhydene.2019.10.077.
584 [51] Bates L, Bradley D, Paczko G, Peters N. Engine hot spots: Modes of auto-ignition and reaction
585 propagation. Combust Flame 2016;166:80–5. https://doi.org/10.1016/j.combustflame.2016.01.002.
586 [52] Khalid AH, Muhamad Said MF, Veza I, Abas MA, Roslan MF, Abubakar S, et al. Hydrogen port
587 fuel injection: Review of fuel injection control strategies to mitigate backfire in internal combustion
588 engine fuelled with hydrogen. Int J Hydrog Energy 2024;66:571–81.
589 https://doi.org/10.1016/j.ijhydene.2024.04.087.
590 [53] Gao J, Wang X, Song P, Tian G, Ma C. Review of the backfire occurrences and control strategies
591 for port hydrogen injection internal combustion engines. Fuel 2022;307:121553.
592 https://doi.org/10.1016/j.fuel.2021.121553.
593 [54] Lee JT, Kim YY, Lee CW, Caton JA. An Investigation of a Cause of Backfire and Its Control Due
594 to Crevice Volumes in a Hydrogen Fueled Engine. J Eng Gas Turbines Power 2001;123:204–10.
595 https://doi.org/10.1115/1.1339985.
596 [55] Wei H, Xu Z, Zhou L, Zhao J, Yu J. Effect of hydrogen-air mixture diluted with
597 argon/nitrogen/carbon dioxide on combustion processes in confined space. Int J Hydrog Energy
598 2018;43:14798–805. https://doi.org/10.1016/j.ijhydene.2018.06.038.

[56] D. Takahashi, N. Matsubara, A. Yamashita, K. Nakata, Toyota Motor Corporation, Shizuoka / Aichi. Toyota’s Hydrogen-Engine Development to Contribute to Carbon Neutrality. 44th Int. Vienna Mot. Symp., vol. 2,2023-36, 2023.